Tau^{IQ} - A canonical image based algorithm to quantify tau PET scans

Alex Whittington[1] and Roger N. Gunn[1,2]; for the Alzheimer's Disease Neuroimaging Initiative

Affiliations:

1. Invicro LLC

2. Department of Brain Sciences, Imperial College London, Hammersmith Hospital Campus, London, UK

Corresponding author

Alex Whittington PhD,

Invicro LLC

Burlington Danes Building,

Hammersmith Hospital,

Du Cane Road,

London, W12 0NN, UK.

Email: alexander.whittington@invicro.co.uk

Word count: 5221

Abstract

Recently, Amyloid^{IQ} was introduced as a new canonical image based algorithm to quantify amyloid PET scans and demonstrated increased power over traditional SUVR approaches when assessed in cross-sectional and longitudinal analyses. We build further on this mathematical framework to develop a Tau^{IQ} algorithm for the quantitative analysis of the more complex spatial distribution displayed by Tau PET radiotracers. **Methods**: Cross-sectional (N=615) and Longitudinal (N=149) [^{18}F]Flortaucipir data were obtained from ADNI along with necessary adjunct amyloid PET and T1 structural MRI data. A subset of these data were used to derive a chronological tau data set, using Amyloid^{IQ} analysis of associated amyloid PET data to calculate the subjects temporal position in the canonical AD disease process, from which canonical images for the non-specific and specific binding components of [^{18}F]Flortaucipir in AD were calculated. These two canonical images were incorporated into the Tau^{IQ} algorithm that enables the quantification of both global and local tau outcome measures using an imaged based regression and statistical parametric analysis of the initial residual image. Performance of the Tau^{IQ} algorithm was compared with SUVR approaches for cross-sectional analyses, longitudinal analyses and correlation with clinical measures (ADAS-Cog, CDR-SB, MMSE). **Results**: Tau^{IQ} successfully calculated global tau load (Tau$_L$) in all 791 scans analysed (range: [-3.5%,185.2%], m±sd: 23%±20.5%) with a non-zero additional local tau component being required in 31% of all scans (CN=22%, MCI=35%, Dementia=72%). Tau^{IQ} was compared to the best SUVR approach in the cross-sectional analysis (Tau$_L$ increase in effect size: CN-vsCN+ [+45%], CN-vsMCI+ [-5.6%], CN-vsDementia+ [+2.3%]) and correlation with clinical scores (Tau$_L$ increase in r^2: CDR-SB +7%, MMSE +38%, ADAS-Cog + 0%). Tau^{IQ} substantially outperformed SUVR approaches in the longitudinal analysis (Tau^{IQ} increase in power: CN+ > 3.2-fold, MCI+ > 2.2-fold, Dementia+ > 2.9-fold). **Conclusions:** Tau$_L$ as calculated by Tau^{IQ} provides a superior approach for the quantification of tau PET data. In particular, it provides a substantial improvement in power for longitudinal analyses and the early detection of tau deposition and thus it should have significant value for clinical imaging trials in AD that are investigating the attenuation of tau deposition with novel therapies.

Introduction

Tau and amyloid-β (Aβ) are the two pathological hallmarks of Alzheimer's Disease and consequently represent two key targets for both drug and biomarker development. The development of Aβ PET biomarkers and their associated analytics is well advanced with established F-18 FDA approved radiotracers ([^{18}F]Florbetapir, [^{18}F]Florbetaben and [^{18}F]Flutemetamol) available on following the pioneering work with [^{11}C]PIB that originated in 2004[1]. In parallel, analytical approaches for Aβ agents have advanced from historical SUVR methods, to the development of Centiloids which allows for conversion of different amyloid agents onto a common scale facilitating their combined use in multi-centre imaging trials[2]. Further, our previous work employing spatiotemporal modelling of Aβ accumulation in AD[3] deduced that amyloid accumulation is a global process that can be characterised by a single parameter (Amyloid Load: $Aβ_L$) and opened the door for the canonical image based quantification employed by Amyloid^{IQ}, which has shown increased power over SUVR based methods in both cross-sectional and longitudinal analyses[4].

The development of tau imaging agents faced increased challenges, due to lower target density, selectivity issues over off-target species and the existence of different isomeric forms of tau (3R,4R), and only gained traction in the following decade with the introduction of [^{18}F]Flortaucipir in 2013[5]. Following this breakthrough, other tau imaging agents have been developed that all demonstrate the ability to measure tau deposition in human subjects including [^{18}F]MK-6240[6], [^{18}F]GTP-1[7], [^{18}F]RO-948[8], [^{18}F]PI-2620[9] and [^{18}F]APN-1607[10] and in May 2020 [^{18}F]Flortaucipir was FDA approved as a radioactive diagnostic agent for adult patients with cognitive impairment who are being evaluated for Alzheimer's disease[11,12].

To date analytical approaches for static tau PET imaging have focussed on SUVR approaches with tau relevant ROIs being employed to quantify the level of tau deposition in regions corresponding to the different stages of tau accumulation described in the post-mortem work of Braak and Braak[13]. This includes the use of regions that correspond to Braak stages I-VI and meta-ROIs which consider the initial/strongest areas of deposition (the transentorhinal cortex and other temporal regions[13]) such as the temporal Jack meta ROI[14]. These SUVR methods have been

applied to cross-sectional(*15–18*) and longitudinal data(*14,19–21*) to show increase in tau signals associated with disease progression in AD.

The present work extends the prior analytical concepts of Amyloid^{IQ} further to account for the more complex spatiotemporal distribution of tau to develop an algorithm for the quantification of tau PET scans (Tau^{IQ}). Initial investigations of tau PET scans had identified that the accumulation in many subjects was more complex with evidence of additional hot spots of local tau deposition. This has led to the development of an algorithm that can accurately quantify both the global tau accumulation pattern (as with amyloid) and any additional subject-specific localised deposits sitting on top of this pattern. The work first describes the development of the Tau^{IQ} algorithm and then provides a comparison of its performance with SUVR approaches for cross-sectional analyses, longitudinal analyses and correlation with clinical measures using [^{18}F]Flortaucipir data obtained from ADNI.

Materials and Methods

Imaging data

Imaging data were obtained from the ADNI database(*22*) (adni.loni.usc.edu). ADNI was launched in 2003 as a public-private partnership, led by Principal Investigator Michael W. Weiner, MD. The primary goal of ADNI has been to test whether serial MRI, PET, other biological markers, and clinical and neuropsychological assessment can be combined to measure the progression of mild cognitive impairment and early AD. For up-to-date information, see www.adni-info.org.

Data for the development of the Tau^{IQ} canonical images

Baseline [^{18}F]Flortaucipir PET, [^{18}F]Florbetapir PET and structural T1-MRI scans were obtained for 233 subjects (127 CN, 82 MCI and 24 Dementia, Gender:118 Male and 114 Female, Age: 76.4 ($\pm$7.0) years with range = [61.3, 94.4], CDR-SB:0.88 ($\pm$1.12) range = [0, 5.5], MMSE:26.7 ($\pm$1.7) range = [20 30], ADAS-Cog:16.4 ($\pm$8.7) range = [2, 52.0])

Cross-sectional testing data

382 additional ADNI subjects were added to the development dataset to create a more comprehensive dataset for testing consisting of a total of 615 subjects (382 CN, 175 MCI and 58 Dementia , Gender:290 Male and 325 Female, Age:74.1($\pm$7.7) years with range = [56.0, 94.4], CDR-SB:0.77 ($\pm$1.28) range = [0, 8], MMSE:28.5 ($\pm$2.0) range = [17, 30], ADAS-Cog:16.0 ($\pm$8.1) range = [2, 52]). For these additional subjects, a [^{18}F]Flortaucipir scan, a static Amyloid PET ([^{18}F]Florbetapir and [^{18}F]Florbetaben) scan and a structural T1-MRI were obtained.

Longitudinal testing data

149 subjects from the cross-sectional dataset (88 CN, 43 MCI, 18 Dementia, Gender: 76 Male and 72 Female, Age:74.5 ($\pm$7.4) years with range = [56.3, 92.2], CDR-SB:0.89 ($\pm$1.42) range = [0, 8], MMSE:28.2 ($\pm$2.3) range = [17, 30], ADAS-Cog:16.5 ($\pm$8.5) range = [5.3, 44.7] at baseline) also had sequential [^{18}F]Flortaucipir PET scans (one or two follow-up visits: 121 subjects had one follow-up scan and 27 had two follow-up visits), between 4 months and 2 and half years after baseline which were used for the longitudinal analysis.

Image Acquisition and Pre-Processing

All human PET data acquisition was performed in accordance with the standardised ADNI protocol(*23*). [18F]Flortaucipir PET scans consisted of emission data from a 30 min (6x5min frames) acquisition at 75 min post-injection and the injected dose was 370 MBq (±10%). [18F]Florbetapir data consisted of emission data from a 20 min (4x5min frames) acquisition collected 50 minutes post-injection and the injected dose was 370 MBq (±10%). [18F]Florbetaben data consisted of emission data from a 20 min (4x5frames) acquisition collected 90 minutes post-injection and the injected dose was 300 MBq (±10%). There were 3 image pre-processing steps applied to the data prior to entry into the ADNI imaging database (For full details, see http://adni.loni.usc.edu/methods/pet-analysis/pre-processing). Briefly, the frames are co-registered and averaged. The resulting image is converted to a 160x160x96 voxel static image with voxel dimensions of 1.5mmx1.5mmx1.5mm. Finally, a gaussian filter (of up to 6mm) was applied in order to harmonise the image resolution to the lowest resolution scanner used in the study. All subjects also underwent a T1-weighted structural MRI. These primary PET and MRI data were downloaded from the ADNI database and used in the subsequent analyses.

Image Processing

Registration of images into stereotactic space - [18F]Flortaucipir, [18F]Florbetapir, [18F]Florbetaben data were nonlinearly registered into MNI152 space(*24*) using the subjects T1-MR scan as part of a diffeomorphic nonlinear registration (DARTEL)(*25*). Initially, the structural MRI images were segmented into grey matter and white matter using SPM12. DARTEL then uses these tissue probability maps to create flow-fields which provide the parameters required to spatially normalise any images which are co-registered to the MRI image into MNI152 space. Each PET image was registered to the corresponding MRI using a rigid-body registration and the individuals' DARTEL flow-field was applied without modulation resulting in [18F]Flortaucipir, [18F]Florbetapir and [18F]Florbetaben images in MNI152 space. The normalised maps were spatially smoothed (8mm full width at half maximum (FWHM) Gaussian kernel).

Generation of SUVR images - SUVR images for [18F]Flortaucipir were generated using the ventrolateral cerebellum of the CIC atlas(*26*) as the reference region by dividing all intensities in the image by the mean uptake value for the ventrolateral cerebellum ROI.

Development of the Tau^{IQ} algorithm

Creation of a chronological [18F]Flortaucipir dataset and derivation of canonical images

For each subject in the development dataset, Amyloid^{IQ} was performed on the subjects' [18F]Florbetapir scan to obtain the subjects' Amyloid Load (Aβ_L). Using a previously published functional form, F, describing the temporal accumulation of Aβ_L in AD(*27*) it was possible to derive the time, T, through the amyloid accumulation process as T = F^{-1}(Aβ_L) which lies in the interval of 0 to 30 years. This process was repeated for all subjects to produce an estimated time for each of them in the amyloid accumulation process. These times were subsequently associated with each subjects' corresponding [18F]Flortaucipir tau PET scan (Figure 1A).

Next, a linear regression was fitted at the voxel level to the chronological [18F]Flortaucipir PET data set to estimate the canonical images (**K** and **NS**). The intercept of the linear regression is the **NS** value for that voxel and the carrying capacity **K** is 30 multiplied by the gradient so that a scan with 100% global tau load (Tau$_L$) will correspond to a subject with the expected level of tau observed at the 30 year time point in the amyloid accumulation process (Figure 1B). In a final step the carrying capacity image was made symmetrical by averaging the intensities in the left and right hemispheres.

The Tau^{IQ} algorithm

The Tau^{IQ} algorithm decomposes a tau PET scan into non-specific, global tau load (Tau$_L$), local tau load (LTau$_L$) and noise using the two canonical images (**NS, K**) and a statistical parametric analysis of an initial residual image (Figure 3). This process is performed in two steps. Firstly, an image based regression of the tau PET scan with the two canonical images is performed in MNI152 space, using QR decomposition in MATLAB, to estimate the Tau$_L$, the non-specific scaling factor (ns) and a residual image,

$$\textbf{SUVr} = ns\,\textbf{NS} + Tau_L\textbf{K} \tag{1}$$

This step is equivalent to Amyloid^{IQ}(*4*) and employs DARTEL(*25*) in the same way to align images into MNI152 space.

Secondly, the derived residual image is processed via a statistical parametric analysis to estimate an image representing the local tau signal (i.e. signal that is over and above the level of noise expected in the residual image). This statistical parametric analysis uses data derived from a set of amyloid negative healthy control [^{18}F]Flortaucipir scans (N=65), where it is assumed that there is negligible tau, to derive mean and standard deviation images from this set of residual images in order to characterize the noise distribution. These mean and standard deviation images allow for the conversion of a residual image calculated by the first step of Tau^{IQ} to a Z-score image. This Z-score image is then processed with the SPM gaussian random fields algorithm(*28*) to estimate clusters of voxels which are significantly greater than zero using a conservative threshold of p<0.01. The LTau$_L$ parameter is then calculated as the 3D integral of the signal in the local tau image and so it is a function of both the intensity and the extent of the local tau signal and has the units SUVRcm^3.

Thus, the overall Tau^{IQ} algorithm (Figure 2) takes as its input a 3D tau PET image and corresponding structural MRI to produce three main outputs; the global tau load (Tau$_L$) which is the scaling factor for the carrying capacity image (**K**), the local tau image which shows the local tau signal across the brain and the local tau load (LTau$_L$) which is a summary measure of this local signal accounting for both extent and intensity.

Comparison of Tau^{IQ} and SUVR Quantification

The Tau^{IQ} outcome measure Tau$_L$ was compared to SUVR in a cross-sectional analysis, longitudinal analysis and in terms of its relationship with clinical scores (CDR-SB, MMSE and ADAS-Cog). For all [^{18}F]Flortaucipir scans, spatially normalised SUVR images were used to calculate mean regional SUVR values for 4 regions through the application of Jack meta, Braak I/II, Braak III/IV and Braak V/VI ROIs defined in MNI152 space (see supplemental Figure 1). Amyloid^{IQ} was used to classify each subject as Aβ+ or Aβ- (positive is defined as an Amyloid

Load ($A\beta_L$) greater than 33%(*29*)) to enable subsequent cross-sectional and longitudinal analyses that were stratified for amyloid positivity.

Cross-sectional Analyses – The Hedges' g effect sizes were calculated and compared for group comparisons of CN+ vs CN-, MCI+ vs CN- and Dementia+ vs CN- (+/- indicates amyloid positive or negative) using Tau_L and SUVR outcome measures. A 95% confidence interval on the calculated Hedges' g was estimated using 10,000 bootstrap replicates of the sample, which was also used to calculate the probability that the outcome measure with the highest effect size in each comparison was superior to all others.

Longitudinal Analyses – A linear regression was performed on the change from baseline of the different outcome measures for each subject, with the intercept constrained to zero. The gradient of this linear regression provides the change per year and this was recorded for every subject and all analysis approaches. The distributions of the changes per year for the different clinical groups were plotted and the mean, standard deviation and effect size (mean divided by the standard deviation) were calculated. A 95% confidence interval on the calculated effect size was estimated using 10,000 bootstrap replicates of the sample, which was also used to calculate a probability that the outcome measure with the highest effect size in each clinical group was superior to all others. Finally, the calculated effect size was also used to estimate the sample size required for a clinical trial with an active and placebo arm designed to detect a 25% reduction in tau accumulation in the active arm over 1 year (power=80%, alpha = 0.05).

Relationship to Clinical Scores – To assess the relationship of the outcome measures Tau_L and SUVR with clinical scores of disease severity, all derived at baseline, correlation analysis (Pearson's correlation) was performed with three clinical measures; Clinical Dementia Rating scale (CDR-SB:N=615), Mini-Mental State Examination (MMSE:N=615) and Alzheimer's Disease Assessment Scale—Cognitive Subscale (ADAS-Cog:N=607).

Results

Canonical images

The process of fitting a linear regression at the voxel-level to the chronological dataset was performed successfully and produced two [^{18}F]Flortaucipir canonical images; the tau carrying capacity image **K** and the non-specific binding image **NS** (Figure 3). The carrying capacity image exhibited the highest intensities in the temporal and parietal lobe and the non-specific binding image showed the highest intensities in the striatum which is consistent with some known off-target binding for [^{18}F]Flortaucipir in this region(*30,31*).

Tau^{IQ}

The Tau^{IQ} algorithm was successfully applied to 791 Tau PET scans (488 CN, 226 MCI, 77 Dementia) from cross-sectional and longitudinal data sets and was able to decompose the scans into three key components – non-specific binding, global tau and local tau. Good characterisation of the [^{18}F]Flortaucipir signal was achieved with final residual images reflecting noise as expected (representative examples are shown in Figure 4). Tau$_L$ values estimated across all scans ranged between -3.5% and 185.2% (mean = 21.9% (±20.4%)) and a local tau component was required in 31% of all scans (CN:22%, MCI:35%, Dementia:72%).

Cross-sectional analysis

Tau$_L$ had the highest effect size for the CN- vs CN+ group comparison (p<0.10) and similar effect size to the best SUVR approach for the CN- vs MCI+ (p<0.64) and CN- vs Dementia+ (p<0.44) group comparisons (Tau$_L$ increase in effect size: CN- vs CN+ [+45%], CN- vs MCI+ [-5.6%], CN- vs Dementia+ [+2.3%], Table 1 and Figure 5). Effect sizes between all groups can be found in the supplementary materials (*Supplementary Table 1*).

Longitudinal analysis

The effect size for Tau^{IQ} was greater than for SUVR in all 6 clinical groups investigated with the largest value observed in the MCI+ group (Table 2). For Tau^{IQ}, the greatest mean increases per year were also seen in the MCI+ group (3.61%/yr), followed by the Dementia+ group (2.52%/yr) and the CN+ group (2.01%/yr). This translated to the MCI+ group having the lowest clinical trial sample size (n=213 per arm) required to show a 25% attenuation in the accumulation of tau

deposition over a 1 yr period (power=80%, alpha = 0.05). There were fewer subjects who showed a reduction in tau signal over time with Tau^{IQ} as compared to any of the SUVR measures (34 for Tau_L, 61 SUVR Jack Meta ROI, 68 for SUVR Braak I/II, 57 for SUVR Braak III/IV, 62 for SUVR Braak V/VI, Figure 6).

Correlation with clinical outcome measures

Analysis of the relationship between the clinical outcome measures (CDR-SB, MMSE and ADAS-Cog) with both Tau^{IQ} and SUVR outcome measures demonstrated that Tau_L had the strongest relationship with CDR-SB and MMSE (Figure 7). For ADAS-Cog, the Jack Meta ROI and Tau_L exhibited the equal highest correlation ($r^2 = 0.34$).

Discussion

The work presented extends the canonical image based quantification recently developed for Aβ (Amyloid^{IQ})[7], that has showed increased performance over existing SUVR based approaches, to tau PET imaging. The more complex deposition of tau, as compared to Aβ, in AD subjects necessitates the incorporation of a local tau component in the algorithm (with 31% of subjects analysed in this study requiring the addition of this local tau component).

[^{18}F]Flortaucipir canonical images characterising the non-specific background signal and the global spatial distribution for tau in AD were successfully calculated form a chronological data set. The non-specific image, **NS**, is consistent with [^{18}F]Flortaucipir images observed in Aβ-healthy controls, where tau is absent, demonstrating a homogeneous signal throughout the brain apart from increased uptake in the striatum consistent with known off-target binding of the tracer that has been linked to monoamine oxidases(*32*). The carrying capacity image, **K**, is consistent with post-mortem maps of tau from AD subjects that show increased deposition in line with Braak staging(*13,33*) with areas of the temporal lobe having the highest signal consistent with the earliest deposition of tau in that region. The Tau^{IQ} algorithm presented uses these canonical images to determine an estimate of the global tau load (the scaling factor associated with the canonical tau image) and an estimate of the local tau load (any additional tau signal that sits on top of the global tau component).

The performance of the primary Tau^{IQ} outcome parameter (Tau$_L$) was assessed against current SUVR approaches using common composite ROIs in cross-sectional analysis, longitudinal analysis and correlation with clinical scores. For the cross-sectional analyses and correlation with clinical outcome measures, Tau^{IQ} typically yielded numerically higher performance metrics when compared to the best SUVR approach (frequently the Jack Meta ROI). In the longitudinal analysis, Tau^{IQ} provided a substantial increase in power over all SUVR approaches. Tau^{IQ} also demonstrated a more plausible annual change (CN+:2.0%/yr, MCI+:3.6%/yr, Dementia+:2.5%/yr) that is consistent with increasing deposition. The clinical trial power calculations performed demonstrated that Tau^{IQ} would be powered to detect a 25% reduction in tau accumulation with a two-arm study involving 213 subjects per arm and that a 50% reduction could be detected with 54 subjects per arm. This has significant implications for the use of Tau^{IQ} in clinical trials where tau

imaging is being deployed as a pharmacodynamic endpoint to assess the impact of novel therapies. Further, Tau^{IQ} was significantly superior in detecting early tau deposition as evidenced by the increase in effect size for the CN- vs CN+ cross sectional group comparison (+45%) and the longitudinal data from the CN+ (+324%) and MCI- (+205%) groups, which indicates that Tau^{IQ} could play an important role in the stratification of early AD populations for trial entry.

Whilst Tau_L has been the primary Tau^{IQ} outcome explored in this work, the algorithm also calculates a local tau load parameter if additional local deposition of tau is present. In this study 31% of all scans had a non-zero local tau load and the percentage was higher as disease progressed (CN:22%, MCI:35%, Dementia:72%). This parameter will be investigated further in future work, but it could have value in stratifying subjects into sub-groups for clinical trial analysis and it will be interesting to explore whether these deposits relate more directly to individual clinical deficits of patients.

One limitation of this work is that longitudinal changes in atrophy and their impact on the PET measures have not been considered, however the magnitude of atrophy effects are lower than the changes observed for Tau_L and are present for both Tau^{IQ} and SUVR. Partial volume correction methods could theoretically be applied to both SUVR and Tau^{IQ} approaches and further work will investigate this. Also, the current analysis has used spatially normalized and smoothed images as part of the analytical pipeline. It is possible that, further advantages could be obtained through processing of unsmoothed images in native space for both SUVR and Tau^{IQ}.

Whilst, the work here has employed the tau tracer [^{18}F]Flortaucipir, the algorithm is equally applicable to other tau tracer given the appropriate generation of tracer specific canonical images. Work with the tracer [^{18}F]GTP-1 has also been presented and demonstrated increased performance over SUVR approaches(*34*).

Conclusion

Tau^{IQ} is a canonical image-based algorithm for the quantification of tau PET scans which accounts for the more complex deposition of tau as compared with amyloid. Global tau load as estimated by Tau^{IQ} provides a substantial improvement in power for longitudinal analyses and the early detection of tau deposition over SUVR approaches and should have significant value for clinical imaging trials in AD that are investigating the attenuation of tau deposition with novel therapies.

<u>Disclosures</u>

KEY POINTS:
QUESTION: What is the best way of quantifying Tau PET images?
PERTINENT FINDINGS: The Tau^{IQ} algorithm introduced in this work shows increased performance over standard SUVR approaches. This quantification approach will provide increased performance when using tau imaging as a biomarker in clinical trials leading to either studies with fewer subjects or increased signals.
IMPLICATIONS FOR PATIENT CARE: This algorithm could provide data for important clinical decision making when AD therapies become approved.

References

1. Klunk WE, Engler H, Nordberg A, et al. Imaging brain amyloid in Alzheimer's disease with Pittsburgh Compound-B. *Ann Neurol*. 2004;55:306-319.

2. Klunk WE, Koeppe RA, Price JC, et al. The Centiloid Project: standardizing quantitative amyloid plaque estimation by PET. *Alzheimers Dement*. 2015;11:1-15.e154.

3. Whittington A, Sharp DJ, Gunn RN. Spatiotemporal Distribution of β-Amyloid in Alzheimer Disease Is the Result of Heterogeneous Regional Carrying Capacities. *J Nucl Med* . 2018;59:822-827.

4. Whittington A, Gunn RN. Amyloid Load – a more sensitive biomarker for amyloid imaging. *J Nucl Med* . September 2018.

5. Chien DT, Bahri S, Szardenings AK, et al. Early clinical PET imaging results with the novel PHF-tau radioligand [F-18]-T807. *J Alzheimers Dis*. 2013;34:457-468.

6. Lohith TG, Bennacef I, Vandenberghe R, et al. Brain Imaging of Alzheimer Dementia Patients and Elderly Controls with (18)F-MK-6240, a PET Tracer Targeting Neurofibrillary Tangles. *J Nucl Med*. 2019;60:107-114.

7. Sanabria Bohórquez S, Marik J, Ogasawara A, et al. [(18)F]GTP1 (Genentech Tau Probe 1), a radioligand for detecting neurofibrillary tangle tau pathology in Alzheimer's disease. *Eur J Nucl Med Mol Imaging*. 2019;46:2077-2089.

8. Wong DF, Comley RA, Kuwabara H, et al. Characterization of 3 Novel Tau Radiopharmaceuticals, (11)C-RO-963, (11)C-RO-643, and (18)F-RO-948, in Healthy Controls and in Alzheimer Subjects. *J Nucl Med*. 2018;59:1869-1876.

9. Mueller A, Bullich S, Barret O, et al. Tau PET imaging with (18)F-PI-2620 in Patients with Alzheimer Disease and Healthy Controls: A First-in-Humans Study. *J Nucl Med*. 2020;61:911-919.

10. Hsu J-L, Lin K-J, Hsiao I-T, et al. The Imaging Features and Clinical Associations of a Novel Tau PET Tracer—18F-APN1607 in Alzheimer Disease. *Clin Nucl Med*. 2020;45.

11. Barthel H. First Tau PET Tracer Approved: Toward Accurate In Vivo Diagnosis of Alzheimer Disease. *J Nucl Med* . 2020;61:1409-1410.

12. Mattay VS, Fotenos AF, Ganley CJ, Marzella L. Brain Tau Imaging: Food and Drug Administration Approval of 18F-Flortaucipir Injection. *J Nucl Med* . 2020;61:1411-1412.

13.   Braak H, Braak E. Neuropathological stageing of Alzheimer-related changes. *Acta Neuropathol*. 1991;82:239-259.

14.   Jack Jr CR, Wiste HJ, Schwarz CG, et al. Longitudinal tau PET in ageing and Alzheimer's disease. *Brain*. 2018;141:1517-1528.

15.   Johnson KA, Schultz A, Betensky RA, et al. Tau positron emission tomographic imaging in aging and early Alzheimer disease. *Ann Neurol*. 2016;79:110-119.

16.   Villemagne VL, Fodero-Tavoletti MT, Masters CL, Rowe CC. Tau imaging: Early progress and future directions. *Lancet Neurol*. 2015;14:114-124.

17.   Schöll M, Lockhart SN, Schonhaut DR, et al. PET Imaging of Tau Deposition in the Aging Human Brain. *Neuron*. 2016;89:971-982.

18.   Ossenkoppele R, Schonhaut DR, Schöll M, et al. Tau PET patterns mirror clinical and neuroanatomical variability in Alzheimer's disease. *Brain*. 2016;139:1551-1567.

19.   Pontecorvo MJ, Devous MD, Kennedy I, et al. A multicentre longitudinal study of flortaucipir (18F) in normal ageing, mild cognitive impairment and Alzheimer's disease dementia. *Brain*. 2019;142:1723-1735.

20.   Sintini I, Martin PR, Graff-Radford J, et al. Longitudinal tau-PET uptake and atrophy in atypical Alzheimer's disease. *NeuroImage Clin*. 2019;23:101823.

21.   Harrison TM, La Joie R, Maass A, et al. Longitudinal tau accumulation and atrophy in aging and alzheimer disease. *Ann Neurol*. 2019;85:229-240.

22.   Mueller SG, Weiner MW, Thal LJ, et al. Ways toward an early diagnosis in Alzheimer's disease: The Alzheimer's Disease Neuroimaging Initiative (ADNI). *Alzheimer's Dement*. 2005;1:55-66.

23.   Jagust WJ, Landau SM, Koeppe RA, et al. The Alzheimer's Disease Neuroimaging Initiative 2 PET Core: 2015. *Alzheimer's Dement J Alzheimer's Assoc*. 2016;11:757-771.

24.   Mazziotta J, Toga A, Evans A, et al. A probabilistic atlas and reference system for the human brain: International Consortium for Brain Mapping (ICBM). *Philos Trans R Soc London Ser B*. 2001;356:1293-1322.

25.   Ashburner J. A fast diffeomorphic image registration algorithm. *Neuroimage*. 2007;38:95-113.

26.   Tziortzi AC, Searle GE, Tzimopoulou S, et al. Imaging dopamine receptors in humans with [11C]-(+)-PHNO: Dissection of D3 signal and anatomy. *Neuroimage*. 2011;54:264-

277.

27.   Jack CR, Wiste HJ, Lesnick TG, et al. Brain β-amyloid load approaches a plateau. *Neurology*. 2013;80:890-896.

28.   Friston KJ, Worsley KJ, Frackowiak RS, Mazziotta JC, Evans AC. Assessing the significance of focal activations using their spatial extent. *Hum Brain Mapp*. 1994;1:210-220.

29.   Whittington A, Seibyl J, Gunn RN. P1-472: CALCULATION OF AβL WITH THE IQAβ ALGORITHM ENABLES AUTOMATIC AND REPRODUCIBLE CLASSIFICATION OF [18F]-FLORBETAPIR SCANS. *Alzheimer's Dement*. 2018;14:P503-P504.

30.   Lowe VJ, Curran G, Fang P, et al. An autoradiographic evaluation of AV-1451 Tau PET in dementia. *Acta Neuropathol Commun*. 2016;4.

31.   Marquié M, Normandin MD, Vanderburg CR, et al. Validating novel tau positron emission tomography tracer [F-18]-AV-1451 (T807) on postmortem brain tissue. *Ann Neurol*. 2015;78:787-800.

32.   Vermeiren C, Motte P, Viot D, et al. The tau positron-emission tomography tracer AV-1451 binds with similar affinities to tau fibrils and monoamine oxidases. *Mov Disord*. 2018;33:273-281.

33.   Braak H, Thal DR, Ghebremedhin E, Del Tredici K. Stages of the pathologic process in Alzheimer disease: age categories from 1 to 100 years. *J Neuropathol Exp Neurol*. 2011;70:960-969.

34.   Whittington A, Hesterman J, Sanabria S, Weimer R, Seibyl J, Gunn RN. TauIQ demonstrates increased power for cross-sectional and longitudinal analysis of Tau tracers as evidenced by [18F]Flortaucipir and [18F]GTP1. In: HAI 2020.
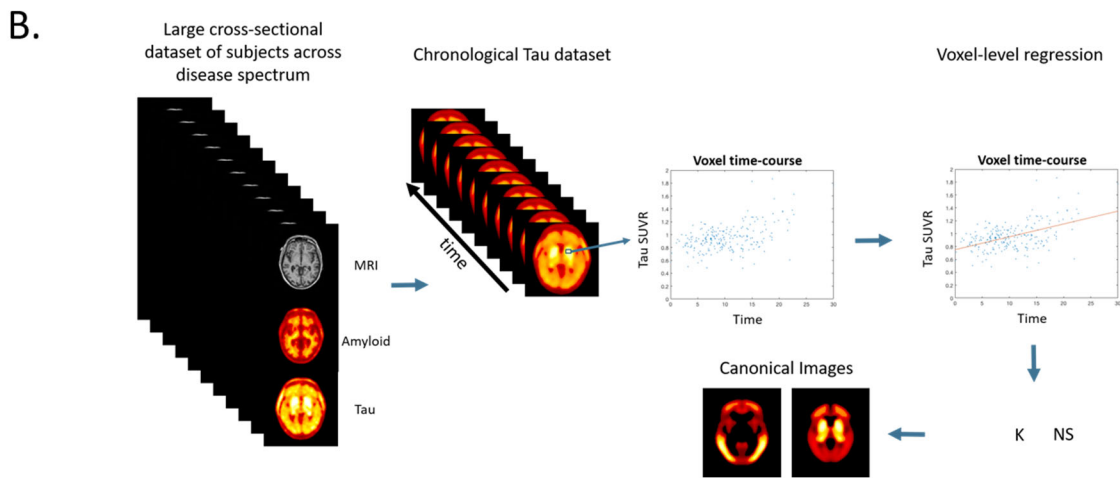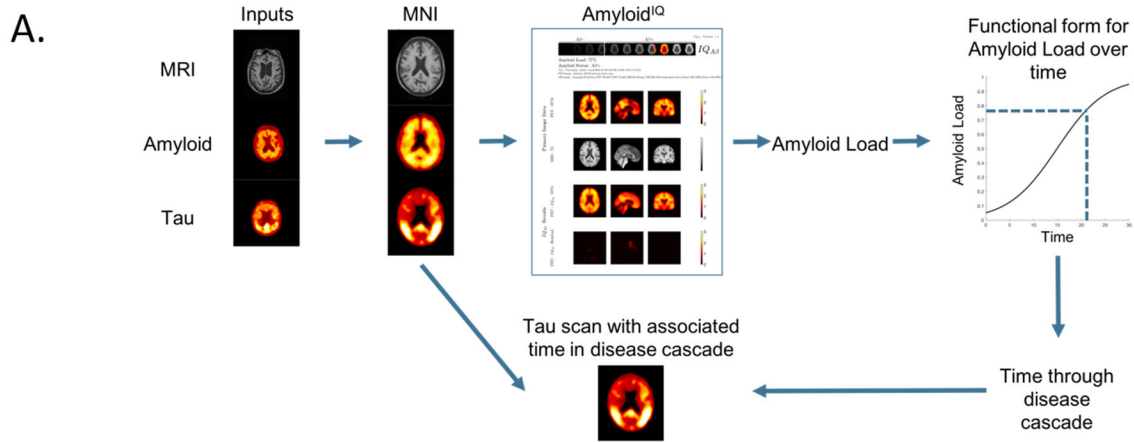
*Figure 1: Methodology for creating [18F]Flortaucipir canonical images - (A) Creation of a chronological [^{18}F]Flortaucipir dataset using associated [^{18}F]Florbetapir data. (B) Generation of [^{18}F]Flortaucipir **K** and **NS** canonical images from voxel-wise modelling of the chronological dataset.*

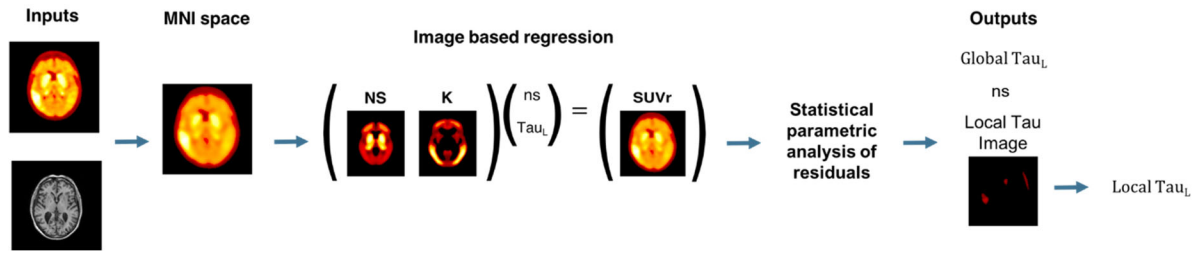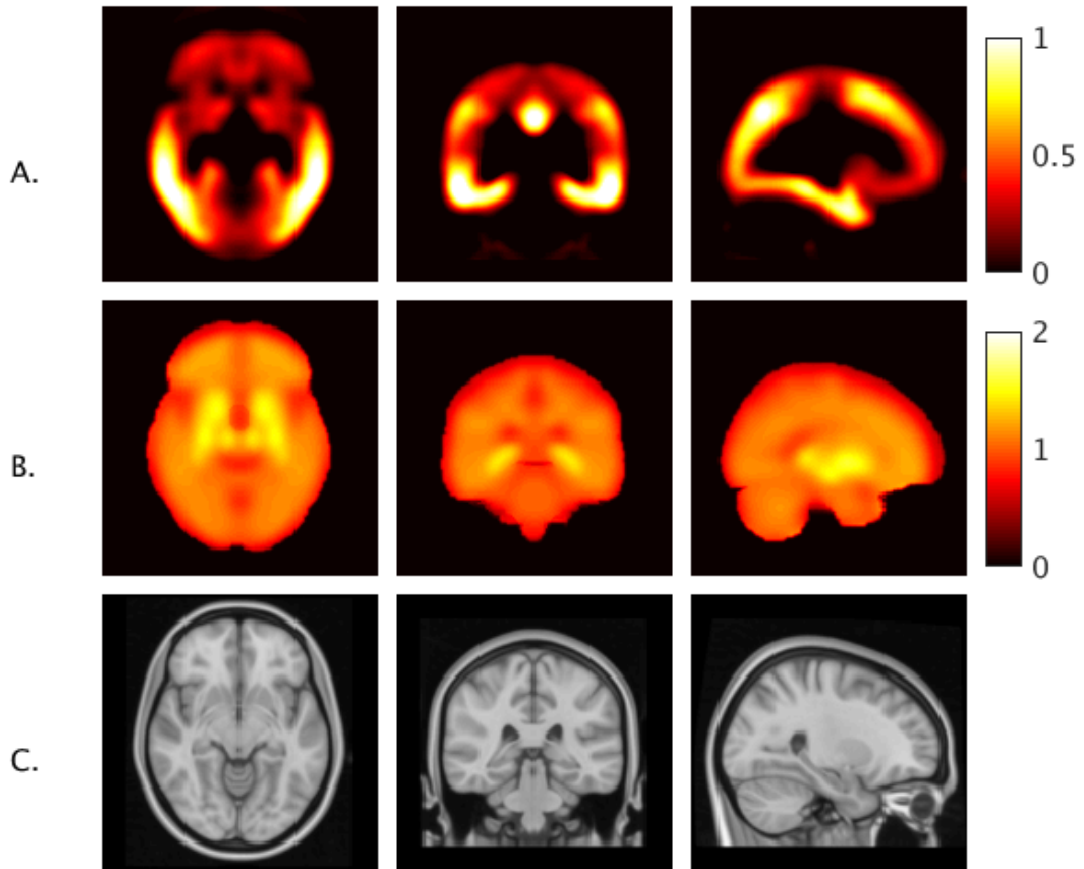*Figure 2: The Tau^{IQ} algorithm which estimates global and local tau outcome measures.*

*Figure 3: Canonical images for [^{18}F]Flortaucipir derived from spatiotemporal modelling of chronological AD data in MNI152 space; A) Tau canonical image (**K**), B) Non-specific canonical image (**NS**) and C) Reference structural T1-MRI image,*
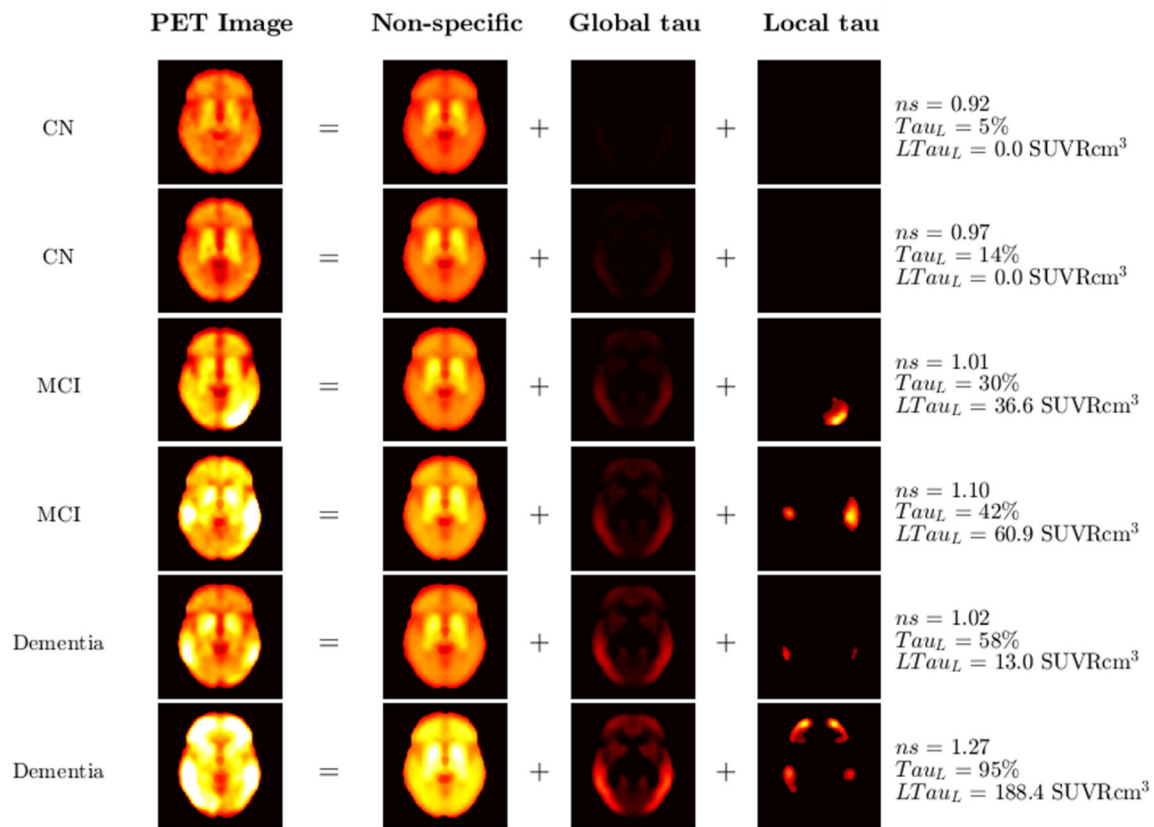
Figure 4: Examples of the Tau^{IQ} decomposition of [^{18}F]Flortaucipir data into non-specific, global and local tau signal.
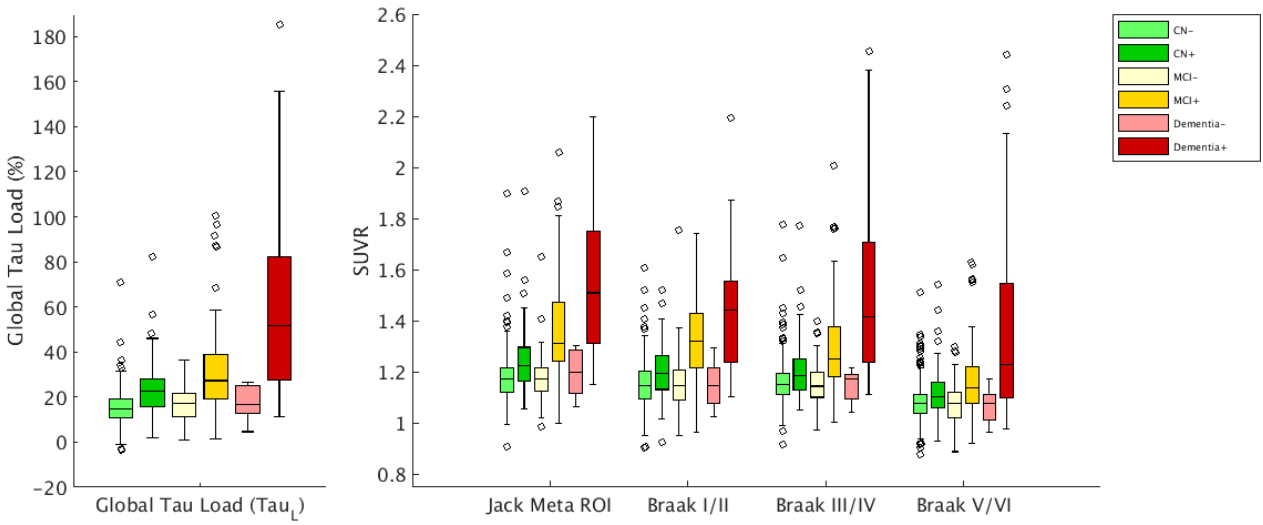
Figure 5: Cross-Sectional Analysis – Boxplots of the distributions of $[^{18}F]$Flortaucipir Tau_L and SUVR outcome measures by clinical group.

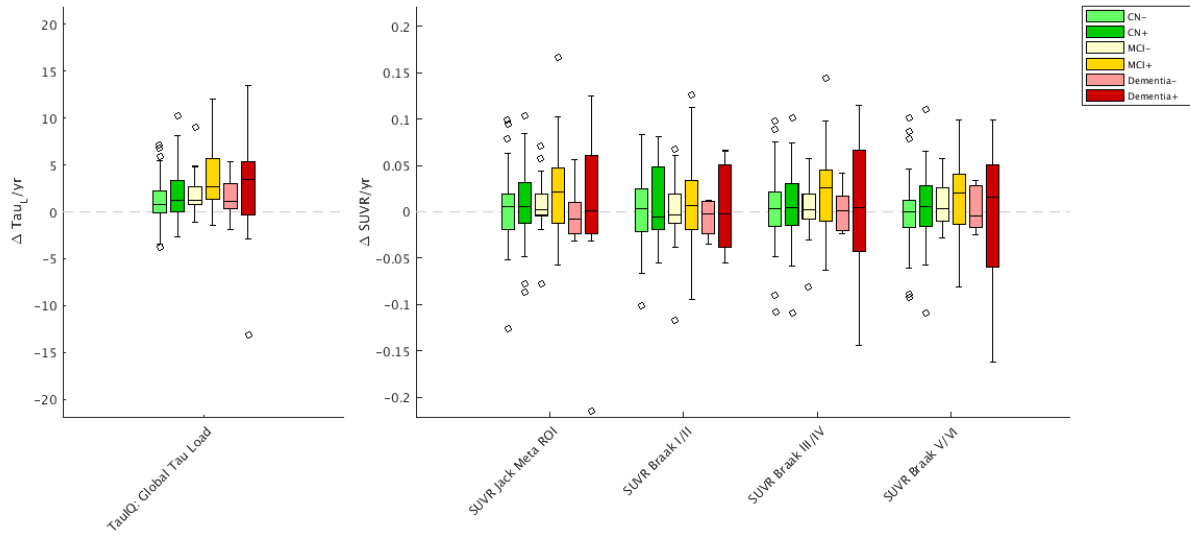*Figure 6: Longitudinal Analysis - Boxplots of the distributions of change in [^{18}F]Flortaucipir Tau$_L$ and SUVR outcome measures.*
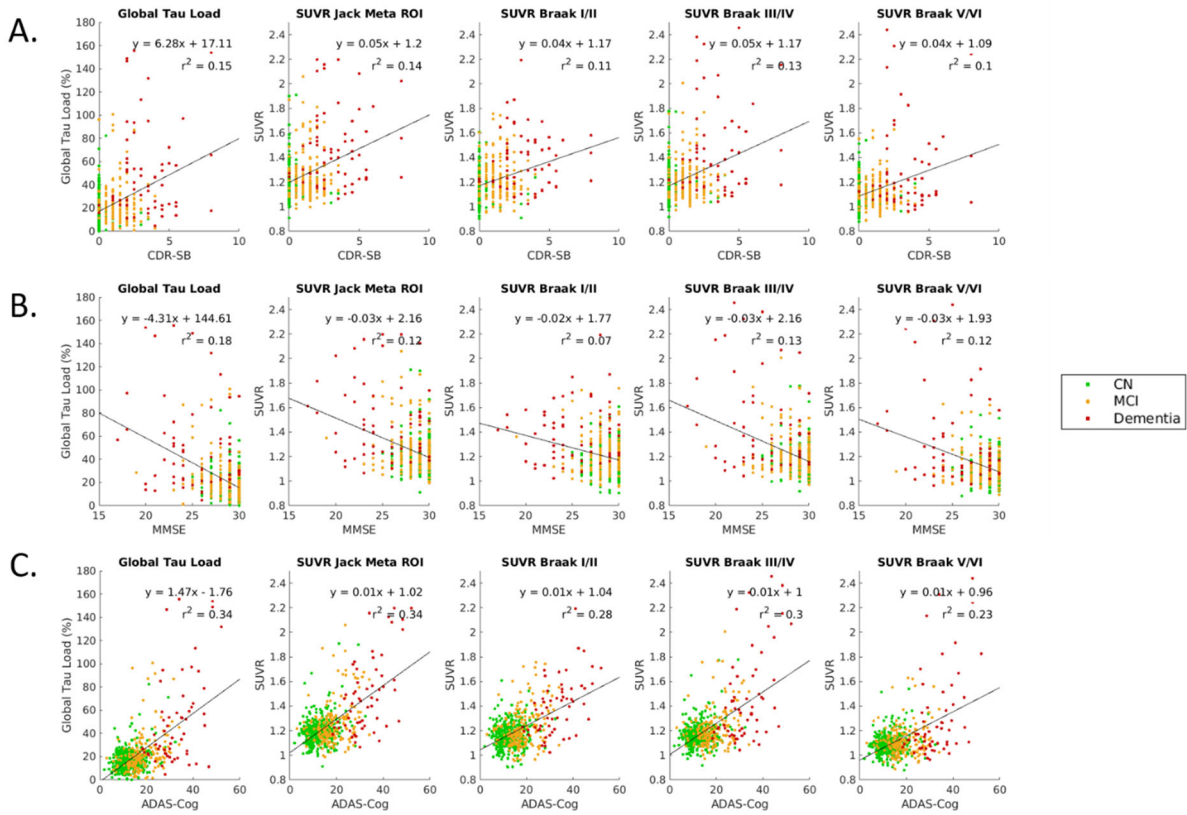
Figure 7: Correlations between clinical scores (CDR-SB, MMSE and ADAS-Cog) and tau imaging outcome measures.

| Outcome Measure	CN- vs CN+	CN- vs MCI+	CN- vs Dementia+
Tau^{IQ} Tau$_L$	**1.00 [0.69,1.35], p<0.10**	1.53 [1.21,1.88]	**2.70 [2.28,3.26], p<0.44**
SUVR Jack Meta ROI	0.69 [0.39,1.03]	1.58 [1.21,2.01]	2.64 [2.16,3.27]
SUVR Braak I/II	0.55 [0.26,0.85]	**1.62 [1.24,2.04] p<0.64**	2.46 [1.98,3.03]
SUVR Braak III/IV	0.57 [0.28,0.88]	1.34 [0.99,1.72]	2.37 [1.93,2.92]
SUVR Braak V/VI	0.49 [0.19,0.80]	0.97 [0.63,1.32]	1.90 [1.48,2.40]

Table 1: Cross-Sectional Analysis – Effect sizes with confidence intervals for [^{18}F]Flortaucipir Tau$_L$ and SUVR outcome measures derived from group comparisons. The best performing method in terms of effect size is highlighted in bold along with the probability it is the best method.

|		Tau^{IQ} Tau$_L$	SUVR Jack Meta ROI	SUVR Braak I/II	SUVR Braak III/IV	SUVR Braak V/VI
CN-	Mean (SD)	**1.20 (2.31)**	0.003 (0.037)	0.001 (0.037)	0.003 (0.036)	-0.001 (0.037)
	Effect Size [CI]	**0.52 [0.28,0.79], p<0.016**	0.09 [-0.18,0.37]	0.02 [-0.25,0.30]	0.08 [-0.19,0.37]	-0.02 [-0.30,0.24]
	n	**940**	33812	557745	37422	847562
CN+	Mean (SD)	**2.01 (2.97)**	0.009 (0.044)	0.007 (0.039)	0.007 (0.041)	0.007 (0.039)
	Effect Size [CI]	**0.68 [0.43,0.98], p< 0.022**	0.21 [-0.12,0.55]	0.19 [-0.15,0.52]	0.18 [-0.16,0.55]	0.17 [-0.16,0.55]
	n	**546**	5726	6699	8170	9019
MCI-	Mean (SD)	**1.87 (2.28)**	0.008 (0.032)	-0.002 (0.040)	0.004 (0.031)	0.010 (0.025)
	Effect Size [CI]	**0.82 [0.57,1.58], p<0.13**	0.24 [-0.22,0.82]	-0.04 [-0.49,0.53]	0.13 [-0.31,0.79]	0.40 [-0.05,0.94]
	n	**377**	4458	190970	14512	1610
MCI+	Mean (SD)	**3.61 (3.31)**	0.023 (0.049)	0.008 (0.052)	0.023 (0.047)	0.017 (0.044)
	Effect Size [CI]	**1.09 [0.79,1.54], p<0.020**	0.47 [0.12,0.85]	0.16 [-0.24,0.57]	0.49 [0.13,0.93]	0.39 [0.00,0.89]
	n	**213**	1130	10229	1063	1655
Dementia-	Mean (SD)	**1.53 (2.43)**	-0.001 (0.032)	-0.007 (0.019)	0.002 (0.024)	0.002 (0.024)
	Effect Size [CI]	**0.63 [-0.13,2.14], p<0.28**	-0.04 [-1.55,0.76]	-0.34 [-1.32,0.76]	0.09 [-1.18,1.01]	0.06 [-1.52,1.01]
	n	**640**	147860	2080	29595	63426
Dementia+	Mean (SD)	**2.52 (6.64)**	0.004 (0.085)	-0.011 (0.079)	0.002 (0.080)	-0.005 (0.078)
	Effect Size [CI]	**0.38 [-0.17,1.42], p<0.27**	0.05 [-0.44,0.83]	-0.13 [-0.58,0.71]	0.02 [-0.56,0.76]	-0.06 [-0.64,0.71]
	n	**1741**	99385	13985	322607	67106

Table 2: Longitudinal Analysis - Change in [^{18}F]Flortaucipir Tau$_L$ and SUVR outcome measures per year for each clinical group. The best performing method in terms of effect size (Mean/SD) is highlighted in bold along with the probability that it is the best method. n is the number of subjects, in both active and placebo arms of a simulated clinical trial, required to show a 25% reduction in tau accumulation in the active arm over a period of 1 year (power=80%, alpha = 0.05).
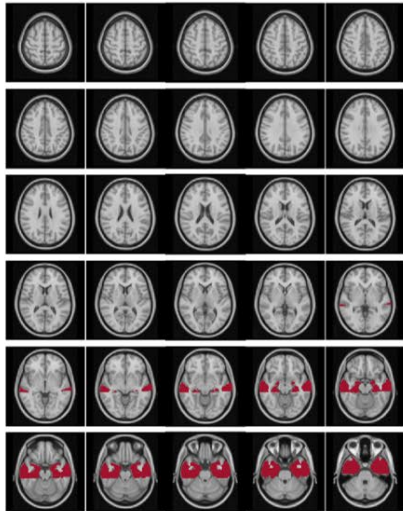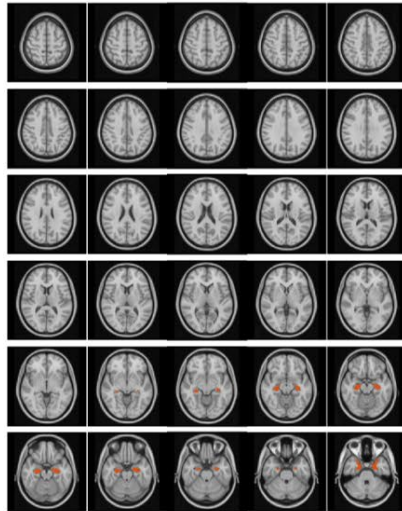
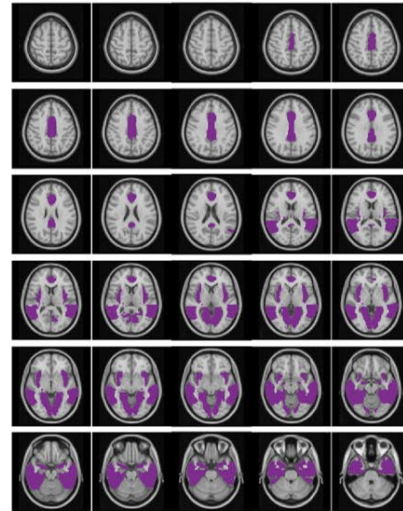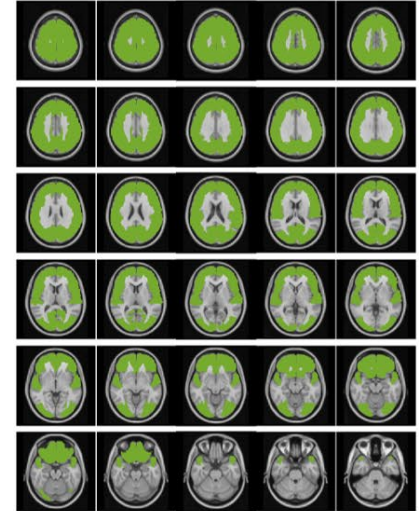| Jack Meta ROI	Braak I/II	Braak III/IV	Braak V/VI

Supplemental Figure 1 - Axial slices of the 4 ROIs used for SUVR analyses.

Cross-Sectional Comparison		Tau-IQ		SUVR			
Group 1	Group 2	Global Tau Load	Local Tau Load	Jack Meta ROI	Braak 12	Braak 34	Braak 56
AD+	AD-	1.10 [0.90, 1.38]	0.82 [0.66, 1.04]	1.19 [0.93, 1.57]	1.35 [0.99, 1.86]	1.07 [0.88, 1.34]	0.86 [0.67, 1.10]
AD+	MCI+	0.90 [0.57, 1.27]	0.77 [0.43, 1.12]	0.77 [0.42, 1.14]	0.55 [0.19, 0.93]	0.81 [0.47, 1.18]	0.77 [0.45, 1.10]
AD+	MCI-	1.81 [1.52, 2.21]	1.27 [0.96, 1.65]	1.94 [1.60, 2.45]	1.86 [1.45, 2.43]	1.71 [1.41, 2.09]	1.33 [1.06, 1.68]
AD+	CN+	1.28 [1.00, 1.63]	1.06 [0.80, 1.37]	1.37 [1.05, 1.79]	1.43 [1.09, 1.88]	1.25 [0.96, 1.61]	1.00 [0.72, 1.31]
AD+	CN-	2.70 [2.27, 3.27]	1.95 [1.50, 2.52]	2.64 [2.16, 3.27]	2.46 [2.00, 3.03]	2.37 [1.92, 2.91]	1.90 [1.49, 2.38]
AD-	MCI+	-0.75 [-1.04, -0.50]	-0.53 [-0.66, -0.41]	-0.88 [-1.23, -0.57]	-1.04 [-1.51, -0.64]	-0.85 [-1.15, -0.61]	-0.71 [-1.05, -0.41]
AD-	MCI-	0.09 [-0.51, 0.70]	-0.13 [-0.27, 0.12]	0.18 [0.43, 0.87]	0.00 [-0.54, 0.61]	-0.04 [-0.54, 0.45]	-0.13 [-0.67, 0.42]
AD-	CN+	-0.54 [-0.95, 0.15]	-0.42 [-0.57, -0.27]	-0.41 [-0.90, 0.07]	-0.43 [-1.00, 0.14]	-0.51 [-0.91, -0.17]	-0.53 [-0.99, -0.10]
AD-	CN-	0.29 [-0.26, 0.85]	-0.08 [-0.16, 0.14]	0.19 [-0.38, 0.77]	0.06 [-0.54, 0.68]	-0.05 [-0.48, 0.34]	-0.17 [-0.68, 0.34]
MCI+	MCI-	1.09 [0.86, 1.37]	0.60 [0.30, 0.91]	1.29 [1.00, 1.63]	1.27 [0.91, 1.71]	1.14 [0.88, 1.44]	0.84 [0.55, 1.12]
MCI+	CN+	0.49 [0.18, 0.78]	0.44 [0.15, 0.68]	0.71 [0.39, 1.05]	0.88 [0.55, 1.25]	0.62 [0.31, 0.94]	0.40 [0.08, 0.71]
MCI+	CN-	1.53 [1.21, 1.88]	0.90 [0.53, 1.31]	1.58 [1.21, 2.01]	1.62 [1.25, 2.05]	1.34 [0.98, 1.72]	0.97 [0.62, 1.31]
MCI-	CN+	-0.74 [-1.04, -0.46]	-0.23 [-0.71, 0.05]	-0.64 [-0.95, -0.34]	-0.43 [-0.79, -0.12]	-0.58 [-0.87, -0.30]	-0.49 [-0.78, -0.19]
MCI-	CN-	0.20 [-0.01, 0.44]	0.09 [-0.12, 0.34]	0.02 [-0.18, 0.24]	0.06 [-0.18, 0.29]	-0.02 [-0.22, 0.20]	-0.04 [-0.25, 0.19]
CN+	CN-	1.00 [0.68, 1.35]	0.39 [0.10, 0.97]	0.69 [0.39, 1.03]	0.55 [0.26, 0.85]	0.57 [0.28, 0.89]	0.49 [0.19, 0.81]

Supplementary Table 1: Effect sizes and 95% confidence intervals for [^{18}F]Flortaucipir Tau$_L$, Local Tau Load and SUVR outcome measures derived from all group comparisons.